

https://dspace.org/

Imaging the African superplume - upper mantle, tomography and moment tensor

Brandt, Martin Barend Christopher

2012-10-01
http://hdl.handle.net/10539/11988

Downloaded from a DSpace repository. https://dspace.org/

Middle Mantle Seismic Structure of the African Superplume

Martin B. C. Brandt[1,2] and Stephen P. Grand[3]

1 Seismology Unit, Council for Geoscience, Pretoria, South Africa martinb@geoscience.org.za, +27-12-841-1199

2 School of Geosciences, University of the Witwatersrand, Johannesburg, South Africa

3 Jackson School of Geosciences, University of Texas at Austin, Austin, Texas, USA steveg@jsg.utexas.edu, +1-512-471-3005

Abstract

We present the results of statistical hypothesis testing of a global tomography model of three-dimensional shear velocity variations for the middle mantle underneath eastern and southern Africa. We apply an F-test to evaluate the validity of a model where a tilted, slow-velocity anomaly in the deepest mantle under southern Africa, known as the African Superplume, is continuous with a slow-velocity anomaly in the upper mantle under eastern Africa. This null hypothesis is tested against alternative hypotheses in which various "obstruction volumes" in the middle mantle are constrained to zero perturbation from the one-dimensional reference velocity during the tomographic inversion. We find that there is an equal probability of accepting an alternative hypothesis with a thin "obstruction volume" at 850–1000 km depth, whereas volumes at other depths are rejected. We conclude that the African Superplume rises to at least 1150 km depth and that the upper mantle slow-velocity anomaly continues from the surface to below the mantle transition zone. We interpret the "obstruction volume" as a weakening of the Superplume in the middle mantle.

Keywords: Global tomography, African Superplume, shear wave, hypothesis testing

Introduction

The African Superplume is a strong shear velocity reduction in the lower mantle beneath southern and eastern Africa (e.g. Simmons *et al*., 2007) which consistently shows up in the 3D mantle S velocity distribution on a global scale (Ritsema *et al*., 1999; Masters *et al*., 2000; Megnin and Romanowicz, 2000; Gu *et al*., 2001; Grand, 2002). The Superplume consists of a ridge-like structure with ultra-low velocity at its base at the core–mantle boundary, a relatively uniform 3% reduction in shear velocity above D" (Helmberger *et al*., 2000), and is orientated roughly NW-SE and tilts towards the east at latitudes from 15° to 30° N. There are strong velocity contrasts at the margins of 2% over ~300 km distance, which suggest a significant compositional change between the Superplume and the surrounding mantle (Ritsema *et al*., 1998a). By forward modelling S, ScS and SKS phases, Ni and Helmberger (2003) estimated that the slow-velocity anomaly extends at least to 1200 km above D". Ritsema *et al*. (1998a) model its top at about 1400 km depth (i.e. about 1400 km above D").

In the upper mantle, a 200 to 400 km wide zone of slow velocities is seen beneath the eastern branch of the East African Rift extending into, but not necessarily through, the mantle transition zone. Shear velocity reductions greater than 3% extend to between 100 to 150 km depth, and velocities ~2.5% slow persist to at least 400 km depth (Ritsema *et al*., 1998b; Nyblade *et al*., 2000). The temperature beneath the rifted lithosphere from 100 to 400 km depth is 140 to 280 K higher than ambient mantle temperatures, consistent with the observation that the 410 km discontinuity in the region is depressed by 30 to 40 km (Venkataraman *et al*., 2004). To explain East African Cenozoic tectonism, one or more upper mantle plume heads have been invoked under the eastern margin of the Tanzania craton (Nyblade *et al*., 2000) or the Afar region (Ritsema and Van Heijst, 2000). Alternatively, passive stretching of the lithosphere may cause small-scale convection beneath the transition from thick cratonic lithosphere to thin oceanic lithosphere or thinned continental lithosphere (King and Ritsema, 2000). Both of these hypotheses can explain the volcanism and gravity field of east Africa, but fail to account for the excess elevation of eastern and southern Africa known as the African Superswell (Lithgow-Bertelloni and Silver, 1998; Forte *et al*., 2010).

To explain the excess elevation of the Superswell a hypothesis has been proposed whereby the African Superplume extends from the core–mantle boundary under southern Africa into the slow-velocity anomaly in the upper mantle under eastern Africa (Ritsema *et al*., 1999; Romanowicz and Gung, 2002). This implies that the African Superplume plays a major role in supplying heat and causing mantle flow in the asthenosphere resulting in hotspot volcanism, and also that deep mantle convection supports the dynamic topography of the African Superswell (Lithgow-Bertelloni and Silver, 1998; Forte *et al*., 2010). However, Ritsema *et al*. (1999) qualify their result: they found a weakening of the slow-velocity anomaly between 670 and 1000 km depth, which they interpret as meaning that the upwelling is obstructed (Figure 1). Backus-Gilbert resolution kernels led them to conclude that the continuity of the slow-velocity anomaly at 2500, 1500 and 700 km depths is not caused by preferential SW to NE body-wave sampling. Other tomography models (e.g., Grand, 2002; Simmons *et al*., 2007) also show a tenuous connection between the deep mantle slow velocities and the upper mantle slow anomalies seen beneath Eastern Africa.

The slow velocities underlying the East African Rift could be either unconnected or linked in a complex way to the deeper Superplume. To put this into context: Global tomographic images have revealed a variety of mantle plumes (Ritsema and Allen, 2003; Montelli *et al*., 2004; Montelli *et al*., 2006). At least nine hotspots, e.g. Ascension, Azores, Canary, Easter, Samoa and Tahiti, cap plumes originating near the core–mantle boundary. But at least another eight, e.g. Bowie, Eastern Australia, Eifel, Etna, Iceland, Cocos-Keeling, Galapagos and Juan de Fuca/Cobb, are associated with plumes whose imaged base is near the 670 km discontinuity. In addition, some plumes exist without associated hotspots, whereas the Reunion and Yellowstone hotspots have no substantial plume underneath. This has led Montelli *et al*. (2004) to suggest two convecting regions in the mantle that are separated by a thermal boundary layer and are linked in a more complex way than either whole or layered convection models.

Global tomography models still lack in detailed resolution. This is apparent in the differences that still exist among models when one compares them in detail (e.g. Gurnis *et al*., 2000; Ritsema *et al*., 1999) (Figure 1). It is true that mantle tomography has improved significantly during the 21st century (e.g. Nolet *et al*., 2007). The African and Pacific Superplumes are now uncontested (see, e.g., Romanowicz and Gung, 2002). Whole-mantle tomography, using traditional ray theory and a large number of different ray trajectories for reflected and transmitted waves in the mantle and outer core with earthquake relocation, has increasingly yielded better images of plumes (e.g. Zhao, 2004). Montelli *et al*. (2004) and Montelli *et al*. (2006) applied finite-frequency tomography, which compensates for the effects of wave diffraction, to the delays of compressional and shear waves in two frequency bands. This method takes into account the sensitivity of travel time to structure away from the ray-theoretical path, which yields better-constrained plume conduits (Nolet *et al*., 2007) and hence detects mantle plumes ~200 km to ~400 km in diameter. But despite these improvements in global tomography the lack in detailed resolution means the nature of convection in the mantle and the behaviour of mantle plumes are still uncertain.

In this article our objective is to investigate in fine detail the connection between the African Superplume and the upper mantle anomaly beneath East Africa by directly testing hypotheses. Previous procedures for estimating reliability and resolution in tomography models include synthetic inversions with random travel-time errors and synthetic inversions on data with travel-time residuals corresponding to a given pattern of mantle heterogeneity, the so called checker board tests (e.g., Grand, 1994). Ritsema *et al*. (1999) have approached resolution by computing Backus-Gilbert kernels for their inversions. These approaches give a good sense of the coverage of data sets in terms of raypaths or sensitivity kernels but are difficult to use in directly assessing hypotheses. A further complication is that source locations are uncertain and it is difficult to include the uncertainty in standard resolution analyses. In our investigation we test hypotheses concerning the continuity between the lower mantle African Superplume and the seismically slow upper mantle beneath East Africa. Each hypothesis is directly tested by

applying a constrained global tomography inversion and seeing if the misfit is significantly degraded statistically.

We apply an F-test to the travel-time residual's variance from numerous test models for a given data set as well as varying a smoothing procedure to allow us to make an objective decision on the truth or falsity of the above mentioned hypotheses. We estimate the sensitivity of our method to lateral model volume size and perform an F-test on the complementary data set to estimate the dependence of our method on changes in the degree of freedom. A midpoint probability plot confirms that even though our data do not follow a normal distribution, they are still valid for hypothesis testing.

Inversion

We added 2,600 new travel time measurements of S, SS, ScS, SKS and SKKS phases to Grand (2002) and Simmons *et al's* (2007) data set of 41,469 phases. These data were derived from earthquakes of magnitude 5.8 to 6.6 for the period 25 October 2007 to 19 November 2008. These earthquakes were recorded by the networks MEDNET (Istituto Nazionale di Geofisica, Italy), GEOSCOPE (Institut de Physique du Globe de Paris), AfricaArray (Pennsylvania State University, USA, The University of the Witwatersrand, South Africa and the South African Council for Geoscience), Global Telemetered Southern Hemisphere Network (USGS Albuquerque Seismological Laboratory, USA), IRIS/IDA (University of California and Scripps Institution of Oceanography, USA), and IRIS/USGS (USGS Albuquerque Seismological Laboratory, USA). The travel-time residuals of measured arrivals versus those predicted by a one-dimensional starting model taken from Grand (1994) were measured to prepare the data for the inversion. The times of the various S phases were found by computing synthetic seismograms using a WKBJ code (Chapman, 1978) and aligning the peaks of the measured data and the synthetics. Earthquake locations were taken from the Harvard Centroid Moment Tensor catalogue, although the depths of the earthquakes were determined by synthetic seismogram modelling of S and sS waves. Shallow earthquakes with depths of less than 39 km were rejected because the S and sS phases became difficult to distinguish and would require more advanced analysis. Corrections for variations in crustal thickness and topography

were made to the synthetic seismograms using the CRUST5.1 model (Mooney *et al.*, 1998). Ellipticity corrections were made for all measured times (Grand, 1994; Simmons *et al.*, 2007).

Next, multiple tomographic inversions were completed with a modified simultaneous iterative reconstruction technique. The mantle was divided into blocks having uniform slowness differences, with dimensions of about 275 x 275 km^2 laterally and with varying depth thicknesses from 75 km to 150 km. The slowness difference for a particular block relative to the starting model is given by the weighted average of the slowness difference associated with each ray that passes through the block. This is only an approximate solution and is applied iteratively using the reconstruction technique to derive the final tomographic model. First, the data were inverted via 25 iterations, allowing only the upper 400 km and bottom 2650–2890 km of the model to vary. After the upper and very deep mantle inversion, the earthquakes were relocated in a least-squares sense using the time residuals from the heterogeneous model derived in the first step. The original data were corrected for the new source locations and the process was repeated until the earthquake locations converged. This is a conservative procedure when estimating middle mantle heterogeneity in that as much of the data variance as possible is explained by upper and very deep mantle variations that are thought to be larger than mid-mantle heterogeneity (Grand, 2002). The resulting shallow three-dimensional model was then used as the starting model for an inversion allowing the whole mantle to vary through 250 iterations. The first upper and very deep mantle inversion was smoothed with a weight of 20 for the central block in relation to the four adjacent blocks (in the shells in 2D) to ensure compatibility with Grand's (1994) previous, conservative models. The second (whole-mantle) inversion was initially also smoothed with a central weight of 20. Smoothing tests with weights of 1, 10, 20, 60 and 120 will be performed below. Note that for a high weight less smoothing occurs.

Three shells and one cross-section from our tomographic model are shown in Plates Aa to d, respectively, labelled REFERENCE. These are the shallowest shell that was inverted twice (25 and 250 iterations), a middle mantle shell at 850–1000 km depth, and the

deepest shell that was also inverted twice and shows the Superplume above the core-mantle boundary. The mean was removed for each shell and the shells were further smoothed (in 3D between shells for map production) at each point with the differences to the six adjacent blocks and then gridded and contoured. Note that the amplitude scale varies with depth so that the velocity differences in the shallowest layers are five times larger than for the deep layers. The cross-section slices through the NW–SE-orientated Superplume along cross-cut 1-1" marked on the maps. For example, the point labelled with "x" is one complex link between the upper and lower anomalies interpreted graphically from cross sections and 3D animations by Begg *et al*. (2009). The scale of the cross-section is the same as those for the shells. Note the near continuity of slow velocity from the deepest mantle to the surface under East Africa.

Hypothesis testing

The tomographic model is derived using an iterative reconstruction technique which minimises the difference between measured and predicted travel-time residuals in a least squares sense. Since the travel-time data are subject to random errors and tomographic images usually need to be smoothed to enhance anomalies, a decision about the truth or falsity of any hypothesis is also subject to the quality and quantity of the data used and to the smoothing constraint used. Where the truth or falsity of a hypothesis is based on experimental evidence, statistical hypothesis testing is often performed to minimise decision errors (e.g. Bain and Engelhardt, 1991; Steyn *et al*., 1999). Hence we construct an F-test to objectively interpret the continuity of the slow-velocity anomaly from the core-mantle boundary to the surface beneath Eastern Africa. The statistical null hypothesis is the model where the Superplume penetrates through the middle mantle (Begg *et al*., 2009). This is written as $H0(Y_0)$: $s_0^2 = s_{0\,min}^2$ where Y_0 is a vector of travel-time residuals explained further below, s_0^2 is the measured-to-predicted travel-time misfits quantified by the residual's variance, and $s_{0\,min}^2$ is the "best-fit" variance for a given data set and smoothing procedure. For hypotheses where the upper and lower mantle anomalies are separated by average mantle slowness between 670 and 1000 km depth, we construct a test model. This is written as $Hm(Y_m)$: $s_m^2 = s_{m\,min}^2$. Y_m and s_m^2 are defined as before for m = 1, 2, 3, … *N*, where m are *N* different volumes of average

mantle slowness situated between the anomalies that we constrain during the tomographic inversion and which we allow to vary. Both "best-fit" variances are defined for the same data set and smoothing procedure, where $s_{0\,min}^2 < s_{m\,min}^2$. We determine how valid the derived test model is by calculating the probability of accepting false, alternative hypotheses. This is an expansion of Ritsema *et al.*'s (1999) study. They applied Backus-Gilbert resolution kernels to determine the trade-off between resolution and stability to decide whether the middle mantle velocity structure of the Superplume is resolved.

To test the alternative hypotheses we followed the same inversion procedure as described above, except that the slowness difference for each block inside an "obstruction volume" was constrained to be zero during the whole-mantle iterative reconstructions. We accomplished this by inverting with the perturbed ray segments that pass through these blocks set to zero. The inversion result for model BLOCK-10 is shown in Plate Ba. Our convention is that BLOCK-10 refers to constraining the perturbation in a volume in the 10th spherical layer from the top in our global tomography model to be zero. In this case slowness anomaly from 850 to 1000 km depth is constrained to be zero. Map-production procedures cause the volume to show up as a "yellow" area. The corresponding cross-sections 1 and 2 are shown in Plates Bb and c. The blocks inside the "obstruction volume" are in "black". In testing models we constrain velocity from 13° S to 28° N and 26° to 48° E for shallow depths and from 18° S to 18° N and 16° to 42° E for deep depths. The postscript S in model names refers to deep tests between 850 and 1600 km with different lateral extend. This area covers the African Superplume below 1300 km depth. Volume depths for the various tests are summarised in Table 1. Plates Ca to f show cross-sections 1 and 2, respectively, for BLOCK models 06-07, 09-10-11 and 13-14-S.

After tomographic inversions for both the null and alternative hypotheses had been completed, we defined vectors $Y_0=y_1,\ldots,y_{n0}$ and $Y_m= y_1,\ldots,y_{nm}$ for the relevant travel-time residuals from the rays that have sampled the m^{th} volume, where m is the corresponding BLOCK model. Since all the volumes are thin in comparison with the mantle thickness, we gave equal weight to each travel-time residual, even if the specific

ray merely grazed the volume. For a simple single-variable test where Y_0 and Y_m are independent, have normal distributions with respective sample variances S_0 and S_m, standard deviations σ_0 and σ_m and degrees of freedom $v_0=n_0-1$ and $v_m=n_m-1$, the F-ratio has the form (e.g. Bain and Engelhardt, 1991; Steyn *et al*., 1999):

$$F(v_0, v_m) \sim \frac{S_0^2 \sigma_m^2}{S_m^2 \sigma_0^2}$$

Evaluating F provides a test of significance between two estimates of sample variances: $F \sim f(n_0-1, n_m-1)$ if $H0(Y_0)$: $s_0^2 = s_{0\ min}^2$ is true. Ray paths through the mantle, excluding the volume, are the same for both respective models. Hence the number of travel-time residuals is $n=n_0=n_m$ and thus $v=v_0=v_m$. If we are 95% confident that the ratio σ_0/σ_m is being exceeded, then this can be written as:

$$P\left[\frac{S_0^2 \sigma_m^2}{S_m^2 \sigma_0^2} \leq f_{0.95}(v_0, v_m)\right] = 0.95$$

We know that all the respective travel-time residual vectors Y_0 and Y_m have variance s_0^2 less than s_m^2. Hence $H0(Y_0)$: $s_0 < Hm(Y_m)$: s_m is always true. For this study we perform an F-test for a left-tailed, type II error to determine the probability of accepting a false alternative hypothesis within the 5% confidence interval around the test parameter s_0^2/s_m^2. A large probability casts doubt on the validity of the null hypothesis (50% means equal probability for both models), whereas a wide confidence interval around s_0^2/s_m^2 corresponds to a poor estimate (e.g. Bain and Engelhardt, 1991; Steyn *et al*., 1999).

Our objective is to statistically quantify whether a connection between the lower mantle African Superplume and the slow upper mantle beneath East Africa is required by the seismic data. This differs from the approach adopted by Hearn (1984) who used an F-test to test the statistical significance of changing the degree of freedom by adding new parameters to his southern California crustal model. For our study, however, determining the degree of freedom is impractical. Our global model currently has 50,996 travel-time measurements versus 99,146 blocks, in comparison with 2,773 blocks for the southern California crust. Smoothing increases the degree of freedom to ~50,996–99,146/6 when accounting for the number of damping equations, although the central smoothing weight is also important. We consider only relevant travel-time residuals, which makes it

difficult to estimate the degree of freedom for each specific hypothesis test. However, all the BLOCK models are thin in comparison with the mantle thickness and have lateral sizes that include only the slow-velocity anomaly. The number of travel-time residuals (only relevant rays) is sufficiently large in comparison with the number of blocks corrected for smoothing, p_0, for both the null hypothesis and the mantle without the respective "obstruction volume", p_m, so that for a thin small volume $p_0 \sim p_m$. Hence $F \sim f_{0.95}(n_0-p_0,n_m-p_m) \sim f_{0.95}(n-1,n-1) \rightarrow f_{0.95}(\infty,\infty) = 1$. We can approximate the 5% confidence interval by a simple, single-variable test. Tests for volume thickness, smoothing and lateral size are performed below with complementary hypothesis testing to estimate sensitivity to the degree of freedom.

Histograms of travel-time residual vectors are shown in Figures 2a to d for REFERENCE (left) and BLOCK (right) models 06-07, 09-10-11, 10 and 13-14-S. Volume depths for the various tests are summarised in Table 1. The corresponding shells and cross-sections are shown in Plates Ba to c and Ca to f. The number of residuals and various "best-fit" parameters are listed with the probabilities and confidence intervals. All these tests employed a central smoothing weight of 20. Note that the "best-fit" parameters for the REFERENCE model change slightly for each test because different rays are considered and the amount of travel-time data decreases with smaller volume size and increasing depth. BLOCK-06-07 with "obstruction volume" in the mantle transition zone and BLOCK-13-14-S with its volume in the deeper mantle have probabilities of 7.3% and 6.1%, respectively, of accepting false, alternative hypotheses. These low probabilities with their narrow confidence levels imply that the REFERENCE model is valid for these depths. However, BLOCK-09-10-11 and its thinner model at 850–1000 km depth, BLOCK-10, have respective probabilities of 31.8% and 50.1%. These high probabilities with their small confidence intervals cast doubt on the validity of the null hypothesis at this depth. Our statistical testing indicates that a valid, alternative hypothesis, consisting of an "obstruction volume" of a mere 150 km thickness, may be true with the same probability as the REFERENCE model with a tenuous connection between the deep mantle- and upper mantle slow velocities. Our testing also confirms the validity of the slow velocities in the REFERENCE model for the deep mantle and the mantle transition

zone.

Smoothing and lateral volume size

Our hypothesis tests are based on travel-time data which are subject to random errors. Sources of error include origin time, location and phase pick. In addition, any global tomographic inversion problem is always underdetermined because of the limited geographical distribution of suitable earthquake sources along, e.g., plate boundaries and due to uneven distribution of seismometers, especially the small numbers in the oceans. We apply smoothing with every iterative reconstruction decreasing the degree of freedom. Smoothing, however, could suppress small anomalies and may destroy the fine detail in a large anomaly hence smoothing is important for our study since alternative hypothesis BLOCK-10 is very thin. A decision to accept or reject a hypothesis from an F-test is based on the test parameter s_0^2/s_m^2. In turn, the residual data variance depends on the amount of smoothing. By repeating the whole-mantle inversions for both REFERENCE and BLOCK models with central smoothing weights of 1, 10, 20, 60 and 120, we can estimate the effect of smoothing. Figures 3a and b are example histograms of travel-time residual vectors for models REFERENCE and BLOCK-13-14 smoothed with central weights of 1 and 120, respectively. "Best-fit" parameters and the probability and confidence interval have the same meaning as before. Cross-sections 1 for both respective models are included in Plates Da and Db. Note how "rough" the image of cross-section 1 in Plate Db appears in comparison with that in Plate Da, which was smoothed with a central weight of 1. The results of the smoothing are summarised in Figures 4a and 4b for all the models with their depths listed in Table 1. Variances for the respective REFERENCE models (*stars*), BLOCK models (*crosses*) and probability at 5% significance ×10 (*triangles*) are presented as a function of the central smoothing weight. A trend observed for every REFERENCE and BLOCK model is that variance decreases with less smoothing. Variances are consistently lower for REFERENCE models than for their corresponding BLOCK models. Model BLOCK-07-08-09 at 525–850 km depth has medium probability (20% to 24%), and corresponding thin BLOCK-08's probabilities vary between 36.0 and 44.2%. All probabilities for thick model 06-07-08-09-10 at 400–1000 km depth are very low (< 5%). BLOCK-10 actually has a slightly higher probability

(> 50%) than the null hypothesis for smoothing weights of 1, 10 and 20; for smoothing weights of 60 and 120 the probability remains above 45.1%. Thicker models 09-10-11 and 08-09-10-11-12 have low to medium probabilities. The probability for mantle transition zone model BLOCK-06-07 is much lower than that for shallow model 07-08-09. All the other deep models have lower probabilities and only 12-S goes above 20%. Consistent probabilities for all the weights led us to conclude that smoothing does not adversely affect our hypothesis testing and also demonstrates the advantage of statistical testing to a graphical interpretation of smoothed, tomographic images.

Another important issue is the effect of lateral volume size on the hypothesis testing. Specifically, we need to know how sensitive the outcome is to a volume that extends beyond the slow-velocity anomaly. BLOCK-13-14 has the same lateral size as the shallower models but, due to the Superplume's tilt towards the south-west with depth, the volume extends to outside the plume. The corresponding "best-fit" parameters for REFERENCE and BLOCK models 13-14-S and 13-14 in Figures 2d and 3a and 3b have different values yet have similar, low probabilities. The variances and probabilities for BLOCK-13-14 are plotted on top of the results for 13-14-S with a *dash-dot* line in Figure 4b. The low percentage probabilities indicate that reasonable changes in lateral volume size do not cause significant changes to the statistical probability. This was also confirmed with extended volumes for the other BLOCK models not shown here.

Another clear trend is the probability decrease with volume thickness for a set of models from thin (BLOCK-08, -10, and -12-S) to thick (BLOCK-06-07-08-09-10, 08-09-10-11-12, and 10-11-12-13-14-S) volumes. This raises the question: Are our results merely an artefact of changing the degree of freedom? We therefore performed F-tests for a two-tailed, type I error to determine the probability that the variances of the complementary rays that did not sample the volume are the same for the null (REFERENCE) and alternative hypotheses (BLOCK models) within the 5% confidence interval. A 100% probability means that the complementary variances are identical, whereas a low value implies that the Earth model surrounding the rays that have sampled the volume differs significantly from the inverted model. Graphs corresponding to Figures 4a and 4b are

shown in Figures 5a and 5b in which each test consists of ~48,000 travel-time residuals and ~99,146 minus 140 to 720 blocks. Complementary variances for the respective REFERENCE models (*stars*) and BLOCK models (*crosses*), and the complementary probability at 5% significance ×10 (*triangles*) are presented as a function of the central smoothing weight. The complementary variances are so similar that they plot on top of one another in all the graphs. The complementary probability decreases with smoothing weight and volume thickness for all three sets of tests. For example, the complementary rays for BLOCK-10 have the highest probability of 96.5% for a smoothing weight of 1, and those for BLOCK-06-07-08-09-10 have the lowest probability of 53.0% for a weight of 60. Models 13-14 and 13-14-S, which have different lateral sizes, have complementary variances and probabilities similar to those in Figure 4b. Given the insignificant size of the "obstruction volume" with its surrounding, sampled mantle in comparison with the whole Earth model, we conclude that all the thick volumes cause the tomographic inversion to recover a complementary model, which differs significantly from the inverted model. However, thin volume BLOCK-10 with high complementary probability is not affected by the change in the degree of freedom and hence represents the real Earth.

An F-test assumes samples of data vectors from a normal distribution (e.g. Bain and Engelhardt, 1991; Steyn *et al*., 1999), but this is not the case here. Figure 6 shows the midpoint probability plot of the travel-time residuals of BLOCK-10 for smoothing weights of 1 to 120 plotted on top of one another (dots) in comparison with the 1st and 3rd quartiles of their normal distributions (*dash-dot* lines). The distribution of travel-time residuals deviates for BLOCK-10 (and all the models not shown here) from the normal distribution at high probability in that more travel-time residuals are near the mean and at low probability, in that there are fewer travel-time residuals from outliers. Less smoothing causes the slope of the normal distribution lines to increase and thus the higher the smoothing weight, the closer the data resemble a normal distribution. If we assume a normal error distribution for the raw tomography travel-time residuals, then smoothing not only removes outliers, but also filters out increasingly more well-behaved data with lower weights. The distributions are similar, smooth and nearly symmetrical around the

mean between the variations of maximum and minimum. Since variance is sensitive to outliers (smoothed out) and since the means of the absolute values and the standard deviation are less for the null hypothesis in every test (e.g. Figures 2a to 2d and 3a and 3b), we believe that the F-test is an appropriate technique for our study.

Discussion

As an alternative hypothesis to the African Superplume extending from the core–mantle boundary through the mantle transition zone into the slow-velocity anomaly in the upper mantle we accepted a model with a thin, small "obstruction volume" at 850–1000 km depth with equal probability to the inverted tomographic model. All other tests in Figures 4a and 4b had lower probabilities. Our result agrees with that of Ritsema *et al*. (1999), namely that the Superplume could be weak in the middle mantle, but differs in that we find a very thin weak zone rather than a weakening between 670 and 1000 km depth. We conclude that the African Superplume rises to at least 1150 km depth (more likely to 1000 km) and that the shallow slow-velocity anomaly continues from the surface to below the mantle transition zone.

Our results are in accord with the global catalogue of different mantle plume varieties by Montelli *et al*. (2004). They identified areas where deep mantle plumes occur below hotspots, other areas where plumes only reach the mid mantle, and yet other areas where plumes are confined to the upper mantle. The African Superplume is similar to the first case in that it originates at the core mantle boundary and is capped by the Afar hotspot in eastern Africa. It is different in that the data does not require slow velocities in the middle mantle to connect the two regimes. Alternatively, the Superplume could consist of two separate lower and upper mantle plumes with the upper plume originating below the 670 km discontinuity. This is similar to another variety of plume also capped by hotspots which has its base near the mantle transition zone. However, the "obstruction volume's" thickness of only 150 km and the dynamic, high topography of the African Superswell (Lithgow-Bertelloni and Silver, 1998; Forte *et al*., 2010) argue against a complete separation into two convecting regions.

The seismic velocities inside the Superplume are slower than normal, indicating that the structure may be hotter than the surrounding mantle and/or may include chemical changes (e.g., Simmons *et al*., 2007). Detailed waveform analyses have revealed that the plume possesses a ridge-like morphology and abrupt wave speed reductions near its boundaries. Slow velocities may indicate high temperatures but the morphology and abrupt velocity jumps associated with the structure cannot be easily attributed to temperature variations alone implying potential chemical changes. This hypothesized chemical component means that at least part of the Superplume is denser than the surrounding mantle which slows its rise upward (e.g., Ni *et al*., 2002; Ni and Helmberger, 2003; Ni *et al*., 2005). The thermally-induced density perturbations are greater in magnitude then the chemically-induced implying overall positive buoyancy throughout the Superplume but may be deforming under the influence of its intrinsic negative chemical buoyancy (Simmons *et al*., 2007). Hence, the "obstruction volume" at 850–1000 km depth may be the upper limit to which the Superplume can rise in the mantle. In that case the slow velocities underlying the East African Rift would be unconnected to the deeper Superplume.

Conclusion

We developed procedures for statistical hypothesis testing to investigate whether the travel-time data require that the tilted, slow-velocity anomaly in the deep mantle under southern Africa extends into the slow-velocity anomaly in the upper mantle under eastern Africa. Testing found a thin zone where the S-velocity may be anomalously reduced above the African Superplume and below the mantle transition zone. We determined that the upper mantle slow-velocity anomaly continues from the surface to below the mantle transition zone.

Acknowledgements

The authors wish to thank Nathan Simmons for setting up for our use of his MatTimes[•] code to calculate predicted travel times with a one-dimensional velocity model and to measure the observed phase arrivals. We thank the University of the Witwatersrand, South Africa, for providing administrative support and the Council for Geoscience, South Africa, for granting MBCB study leave to spend time at the University of Texas at Austin.

References

Bain, L. J. and M. Engelhardt, 1992, *Introduction to Probability and Mathematical Statistics*, 2nd ed. The Duxbury Advanced Series in Statistics and Decision Theory, PWS-Kent Publishing Co, Boston, USA, 644 pp.

Begg, G. C., W. L. Griffin, L. M. Natapov, S. Y. O' Reilly, S. P. Grand, C. J. O' Neill, J. M. A. Hronsky, Y. Poudjom Djomani, C. J. Swain, T. Deen and P. Bowden, 2009, The lithospheric architecture of Africa: Seismic tomography, mantle petrology, and tectonic evolution, *Geosphere*, *5*, 23–50.

Chapman, C. H., 1978, A new method for computing synthetic seismograms, *Geophysical Journal of the Royal Astronomical Society*, *5*, *4*, 481–518.

Forte, A. M., S. Quéré, R. Moucha, N. A. Simmons, S. P. Grand, J. X. Mitrovica and D. B. Rowley, 2010, Joint seismic-geodynamic-mineral physical modeling of African geodynamics: A reconciliation of deep-mantle convection with surface geophysical constraints, *Earth and Planetary Science Letters*, *295*, 329–341, doi:10.1016/j.epsl.2010.03.017.

[•] MatTimes: A MATLAB-based seismic travel time calculation and visualisation toolbox The Department of Geosciences at Texas Tech University.

Grand, S. P., 1994, Mantle shear structure beneath the Americas and surrounding oceans, *Journal of Geophysical Research*, 99, B6, 11,591–11,621.

Grand, S. P., 2002, Mantle shear-wave tomography and the fate of subducted plates, *Philosophical Transactions of the Royal Society of London*, *360*, 2475–2491.

Gu, Y. J., A. M. Dziewonski, W. Su and G. Ekstrom, 2001, Models of the mantle shear velocity and discontinuities in the pattern of lateral heterogeneity, *Journal of Geophysical Research*, *106*, 11,169–11,199.

Gurnis, M., J. X. Mitrovica, J. Ritsema and H. van Heijst, 2000, Constraining mantle density structure using geological evidence of surface uplift rate: The case of the African Superplume, *Geochemistry Geophysics Geosystems*, *1*, *1020*, doi:10.1029/1999GC000035.

Hearn, T. M., 1984, Pn travel times in southern California, *Journal of Geophysical Research*, *89*, 1843–1855.

Helmberger, D., S. Ni, L. Wen and J. Ritsema, 2000, Seismic evidence for ultra-low velocity zones beneath Africa and eastern Atlantic, *Journal of Geophysical Research*, *105*, 23,865–23,878.

King, S. D. and J. Ritsema, 2000, African hot spot volcanism: Scale-scale convection in the upper mantle beneath cratons, *Science*, *290*, 1137–1140.

Lithgow-Bertelloni, C. and P. G. Silver, 1998, Dynamic topography, plate driving forces and the African superswell, *Nature*, *395*, 296–272.

Masters, T. G., G. Laske, H. Bolton and A. Dziewonski, 2000, The relative behaviour of shear velocity, bulk sound speed and compressional velocity in the mantle: Implications for chemical thermal structure, in Earth's deep interior. Mineral physics and tomography

from the atomic to the global scale. (*Editors* S. Karato *et al.*), *AGU Geophysical Monograph*, *117*, 63–87. Washington, DC, USA.

Megnin, C., and B. Romanowicz, 2000, The three-dimensional shear velocity structure of the mantle from the inversion of body, surface and higher-mode waveforms, *Geophysical Journal International*, *243*, 709–728.

Montelli, R., G. Nolet, F. A. Dahlen, G. Masters, E. R. Engdahl and S. Hung, 2004, Finite-frequency tomography reveals a variety of plumes in the mantle, *Science*, 303, 338–343.

Montelli, R., G. Nolet, F. A. Dahlen and G. Masters, 2006, A catalogue of deep mantle plumes: New results from finite-frequency tomography. *Geochemistry Geophysics Geosystems*, *7*, Q11007, doi:10.1029/2006GC001248.

Mooney, W. D., G. Laske and T. G. Masters, 1998, CRUST 5.1: A global crustal model at 5°× 5°, *Journal of Geophysical Research*, *103*, 727–747.

Ni, S., E. Tan, M. Gurnis and D. Helmberger, 2002, Sharp sides to the African Superplume, *Science*, *296*, 1850–1852.

Ni, S. and D. V. Helmberger, 2003, Ridge-like lower mantle structure beneath South Africa, *Journal of Geophysical Research*, *108*, *B2*, *2094*, doi:10.1029/2001JB001545.

Ni, S., D. V. Helmberger and J. Tromp, 2005, Three-dimensional structure of the African superplume from waveform modeling, *Geophysical Journal International*, *161*, 283–294.

Nolet, G., R. Allen and D. Zhao, 2007, Mantle plume tomography, *Chemical Geology*, *241*, 248–263.

Nyblade, A. A., T. J. Owens, H. Gurrola, J. Ritsema and C. A. Langston, 2000, Seismic evidence for a deep upper mantle thermal anomaly beneath east Africa, *Geology*, *28*, 599–602.

Ritsema, J., S. Ni, D. V. Helmberger and H. P. Crotwell, 1998a, Evidence for strong shear velocity reductions and velocity gradients in the lower mantle beneath Africa, *Geophysical Research Letters*, *25*, *23*, 4245–4248.

Ritsema, J., A. A. Nyblade, T. J. Owens, C. A. Langston and J. C. VanDecar, 1998b, Upper mantle seismic velocity structure beneath Tanzania, east Africa: Implications for the stability of cratonic lithosphere, *Journal of Geophysical Research*, *103*, 21,201–21,213.

Ritsema, J., H. J. van Heijst and J. H. Woodhouse, 1999, Complex shear wave velocity structure imaged beneath Africa and Iceland, *Science*, *286*, 1925–1928.

Ritsema, J. and Van Heijst, H., 2000, New seismic model of the upper mantle beneath Africa, *Geology*, *28*, 63–66.

Ritsema, J. and R. M. Allen, 2003, The elusive mantle plume, *Earth and Planetary Science Letters*, *207*, 1–12.

Romanowicz, B. and Y. Gung, 2002, Superplumes from the core–mantle boundary to the lithosphere: Implications for heat flux, *Science*, *296*, 513–516.

Simmons, N. A., A. M. Forte and S. P. Grand, 2007, Thermochemical structure and dynamics of the African superplume, *Geophysical Research Letters*, *34*, L02301, doi:10.1029/2006GL028009.

Steyn, A. G. W., C. F. Smith, S. H. C. du Toit and C. Strasheim., 1999, *Modern Statistics in Practice*, 1st ed., Van Schaik, Pretoria, South Africa, 764 pp.

Venkataraman, A., A. A. Nyblade and J. Ritsema, 2004, Upper mantle Q and thermal structure beneath Tanzania, East Africa, from teleseismic P wave spectra, *Geophysical Research Letters*, *31*, L15611, doi:10.1029/2004GL020351.

Zhao, D., 2004, Global tomographic images of mantle plumes and subducting slabs: Insight into the deep Earth dynamics, *Physics of the Earth and Planetary Interiors*, *146*, 3–34.

Table 1

Volume thickness of the BLOCK models

Test model	Depth
BLOCK-06-07	400–650 km
BLOCK-08	650–750 km
BLOCK-07-08-09	525–850 km
BLOCK-06-07-08-09-10	400–1000 km
BLOCK-10	850–1000 km
BLOCK-09-10-11	750–1150 km
BLOCK-08-09-10-11-12	650–1300 km
BLOCK-12-S	1150–1300 km
BLOCK-11-12-13-S	1000–1450 km
BLOCK-10-11-12-13-14-S	850–1600 km
BLOCK-13-14	1300–1600 km
BLOCK-13-14-S	1300–1600 km

The postscript S in model names refers to deep tests between 850 and 1600 km with different lateral extent.

Figure Captions

Figure 1. Vertical cross section to illustrate the African Superplume's slow-velocity anomaly with Backus-Gilbert resolution kernels for locations X, Y, and Z at 2500, 1500, and 700 km depth, respectively, and shells (left, after Figure 4 in Ritsema *et al*., 1999) and obliquely orientated cross sections for seismic tomography model S20RTS (right, after Figure 1 in Gurnis *et al*., 2000).

Figure 2a. Histogram of travel-time residuals for model REFERENCE (left, labelled 0 for vector Y_0) and BLOCK-06-07 (right) smoothed with a central weight of 20. Residuals are grouped into bins of 1 ms. The number of residuals (N) with "best-fit" parameters maximum (max), the mean, mean of the absolute values (|mean|), standard deviation (std), variance (var) and minimum (min) are listed on the inside of the histogram and the probability and confidence interval at the bottom. For graphical presentations of BLOCK-06-07 see Plates Ca and Cd.

Figure 2b. Histogram of travel-time residuals for model REFERENCE (left, labelled 0 for vector Y_0) and BLOCK-09-10-11 (right) smoothed with a central weight of 20. Residuals are grouped into bins of 1 ms. The number of residuals (N) with "best-fit" parameters maximum (max), mean, mean of the absolute values (|mean|), standard deviation (std), variance (var) and minimum (min) are listed on the inside of the histogram and the probability and confidence interval at the bottom. For graphical presentations of BLOCK-09-10-11 see Plates Cb and Ce.

Figure 2c. Histogram of travel-time residuals for model REFERENCE (left, labelled 0 for vector Y_0) and BLOCK-10 (right) smoothed with a central weight of 20. Residuals are grouped into bins of 1 ms. The number of residuals (N) with "best-fit" parameters maximum (max), mean, mean of the absolute values (|mean|), standard deviation (std), variance (var) and minimum (min) are listed on the inside of the histogram and the probability and confidence interval at the bottom. For graphical presentations of BLOCK-10 see Plates Ba to Bc.

Figure 2d. Histogram of travel-time residuals for model REFERENCE (left, labelled 0 for vector Y_0) and BLOCK-13-14-S (right) smoothed with a central weight of 20. Residuals are grouped into bins of 1 ms. The number of residuals (N) with "best-fit" parameters maximum (max), mean, mean of the absolute values (|mean|), standard deviation (std), variance (var) and minimum (min) are listed on the inside of the histogram and the probability and confidence interval at the bottom. For graphical presentations of BLOCK-13-14-S see Plates Cc and Cf.

Figure 3a. Histogram of travel-time residuals for model REFERENCE (left, labelled 0 for vector Y_0) and BLOCK-13-14 (right) smoothed with a central weight of 1. Residuals are grouped into bins of 1 ms. The number of residuals (N) with "best-fit" parameters maximum (max), mean, mean of the absolute values (|mean|), standard deviation (std), variance (var) and minimum (min) are listed on the inside of the histogram and the probability and confidence interval at the bottom. For a graphical presentation of BLOCK-13-14 see Plate Da.

Figure 3b. Histogram of travel-time residuals for model REFERENCE (left, labelled 0 for vector Y_0) and BLOCK-13-14 (right) smoothed with a central weight of 120. Residuals are grouped into bins of 1 ms. The number of residuals (N) with "best-fit" parameters maximum (max), mean, mean of the absolute values (|mean|), standard deviation (std), variance (var) and minimum (min) are listed on the inside of the histogram and the probability and confidence interval at the bottom. For a graphical presentation of BLOCK-13-14 see Plate Db.

Figure 4a. Variances for the respective reference models (*stars*) and BLOCK models (*crosses*) and probability at 5% significance ×10 (*triangles*) as a function of the central smoothing weight. BLOCK models shown are: 08 (top left), 07-08-09 (top middle), 06-07-08-09-10 (top right), 10 (bottom left), 09-10-11 (bottom middle), and 08-09-10-11-12 (bottom right).

Figure 4b. Variances for the respective reference models (*stars*) and BLOCK models (*crosses*) and probability at 5% significance ×10 (*triangles*) as a function of the central smoothing weight. BLOCK models shown are: 12-S (top left), 11-12-13-S (top middle), 10-11-12-13-14-S (top right), 06-07 (bottom left), and 13-14-S (bottom right). The variances and probabilities for model BLOCK-13-14 are plotted on top of those for model BLOCK-13-14-S with a *dash-dot* line.

Figure 5a. Complementary variances for the respective reference models (*stars*) and BLOCK models (*crosses*) and complementary probability at 95% significance ×10 (*triangles*) as a function of the central smoothing weight. BLOCK models shown are: 08 (top left), 07-08-09 (top middle), 06-07-08-09-10 (top right), 10 (bottom left), 09-10-11 (bottom middle), and 08-09-10-11-12 (bottom right).

Figure 5b. Complementary variances for the respective reference models (*stars*) and BLOCK models (*crosses*) and complementary probability at 5% significance ×10 (*triangles*) as a function of the central smoothing weight. BLOCK models shown are: 12-S (top left), 11-12-13-S (top middle), 10-11-12-13-14-S (top right), 06-07 (bottom left), and 13-14-S (bottom right). The complementary variances and probabilities for model BLOCK-13-14 are plotted on top of those for model BLOCK-13-14-S with a *dash-dot* line.

Figure 6. Midpoint probability plot of the travel-time residuals of hypothesis BLOCK-10 for central smoothing weights of 1, 10, 20, 60 and 120 plotted on top of one another (*dots*) in comparison with a normal distribution probability plot (*dash-dot* line). The probability plot slopes become progressively steeper, more closely resembling a normal distribution, with increasing central smoothing weight.

Plate A. Three spherical shells from our global tomography model labelled REFERENCE (a, b and c). The shallowest and deepest shells (a and c) were inverted with 25 iterations before the whole mantle, including the shell at 850–1000 km depth (b), was inverted with 250 iterations. The Superplume is shown above the core-mantle boundary

in red under and surrounding Africa (c). All shells were smoothed with a central weight of 20. An "x" on cross-section 1 (d) indicates the complex link between the slow-velocity anomalies. A relative scale is shown at the bottom (d) for every second layer with every 4th layer numbered: below 650 km and above 2500 km depth the scale is the same for all the layers. Selected cross-sections from cross-cuts 1 and 2 for the various BLOCK models are included in Plates B, C and D. The mean value removed for each shell is shown at the bottom, right.

Plate B. Spherical shell from model BLOCK-10 at 850–1000 km depth (a) smoothed with a central weight of 20. The volume constrained to zero during the inversions is indicated with a yellow block beneath eastern and southern Africa. The volume in (a) constrained to zero during the whole-mantle inversion is indicated in black on cross-sections 1 and 2 (b and c). A relative scale is shown at the bottom (b and c) for every second layer with every 4th layer numbered: below 650 km and above 2500 km depth the scale is the same for all the layers. The mean value removed for the shell is shown at the bottom, right.

Plate C. Cross-sections 1 and 2 for models BLOCK-06-07 (a and d), BLOCK-09-10-11 (b and e) and BLOCK-13-14-S (c and f) smoothed with a central weight of 20. The volume constrained to zero perturbation during the whole-mantle inversion is indicated in black. A relative scale is shown at the bottom (c and f) for every second layer with every 4th layer numbered: below 650 km and above 2500 km depth the scale is the same for all the layers.

Plate D. Cross-section 1 for model BLOCK-13-14 smoothed with a central weight of 1 (a) and a weight of 120 (b). The volume constrained to zero perturbation during the whole-mantle inversion is indicated in black. A relative scale is shown at the bottom (b) for every second layer with every 4th layer numbered: below 650 km and above 2500 km depth the scale is the same for all the layers.

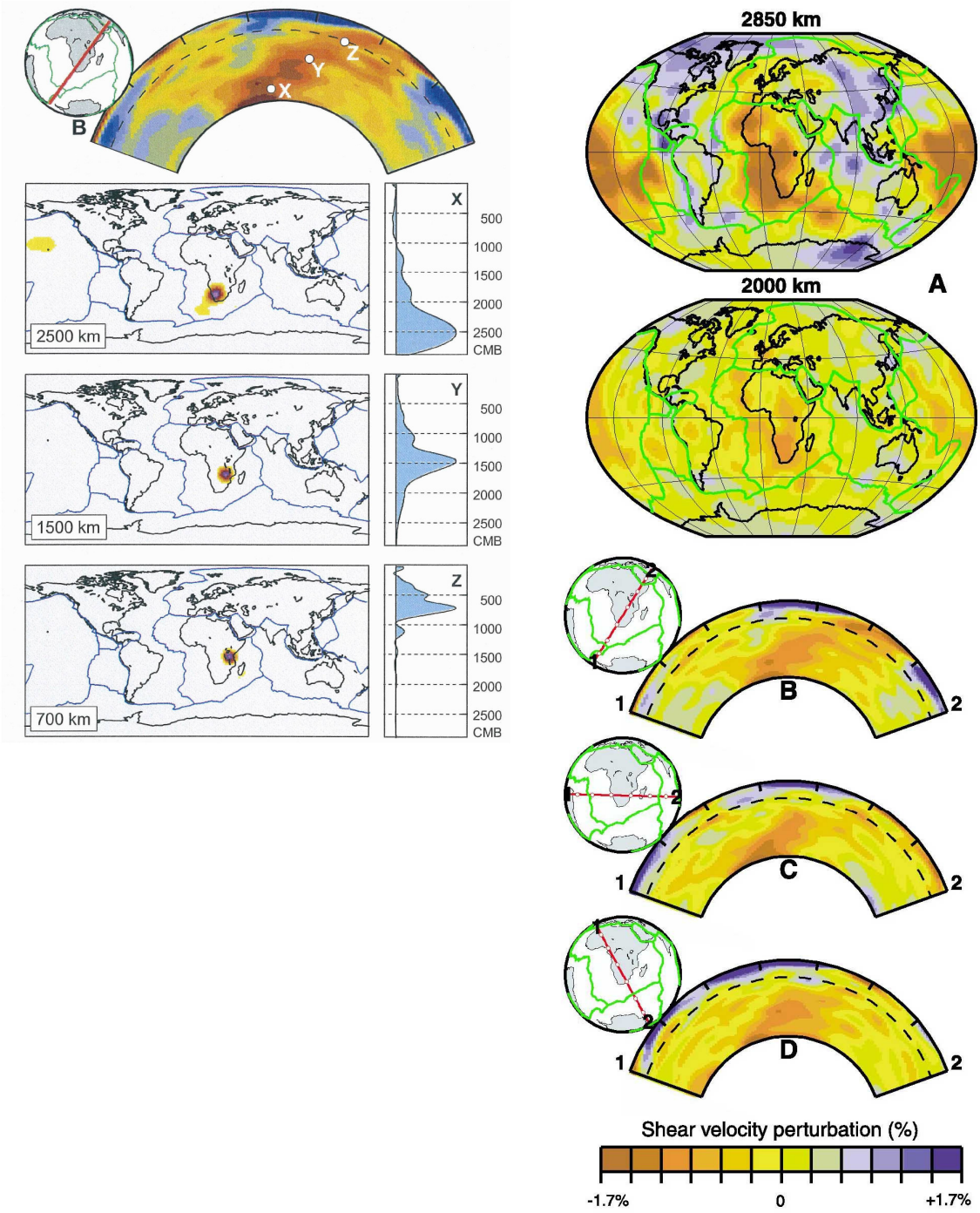

B
Z
Y
X
2500 km
1500 km
700 km
X
Y
Z
500
1000
1500
2000
2500
CMB
2850 km
2000 km
A
B
C
D
1
2
Shear velocity perturbation (%)
-1.7%
0
+1.7%

Figure 1

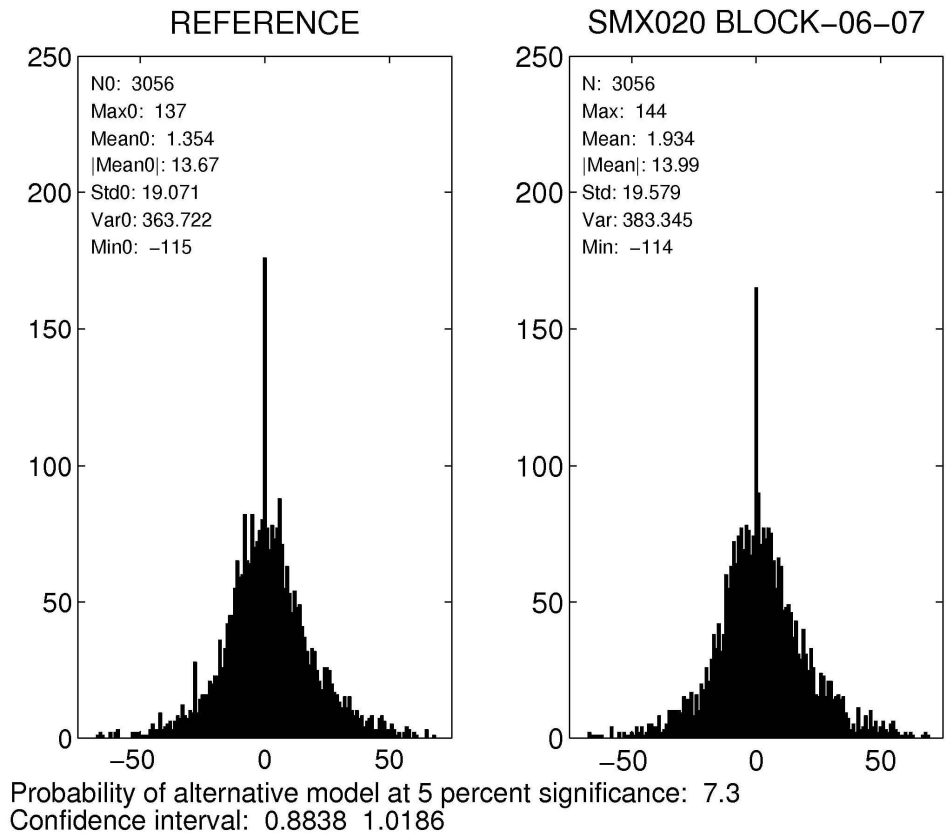

REFERENCE
SMX020 BLOCK−06−07
N0: 3056
Max0: 137
Mean0: 1.354
|Mean0|: 13.67
Std0: 19.071
Var0: 363.722
Min0: −115
N: 3056
Max: 144
Mean: 1.934
|Mean|: 13.99
Std: 19.579
Var: 383.345
Min: −114
250
200
150
100
50
0
−50
0
50
Probability of alternative model at 5 percent significance: 7.3
Confidence interval: 0.8838 1.0186

Figure 2a

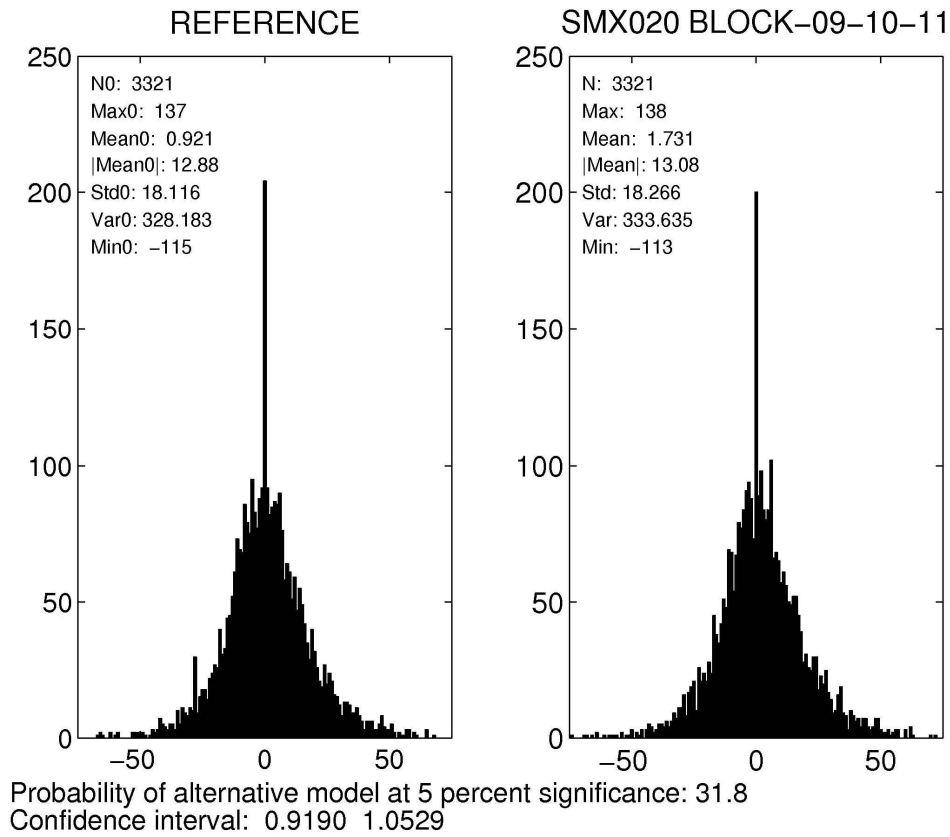

REFERENCE
SMX020 BLOCK−09−10−11
N0: 3321
Max0: 137
Mean0: 0.921
|Mean0|: 12.88
Std0: 18.116
Var0: 328.183
Min0: −115
N: 3321
Max: 138
Mean: 1.731
|Mean|: 13.08
Std: 18.266
Var: 333.635
Min: −113
250
200
150
100
50
0
−50
0
50
Probability of alternative model at 5 percent significance: 31.8
Confidence interval: 0.9190 1.0529

Figure 2b

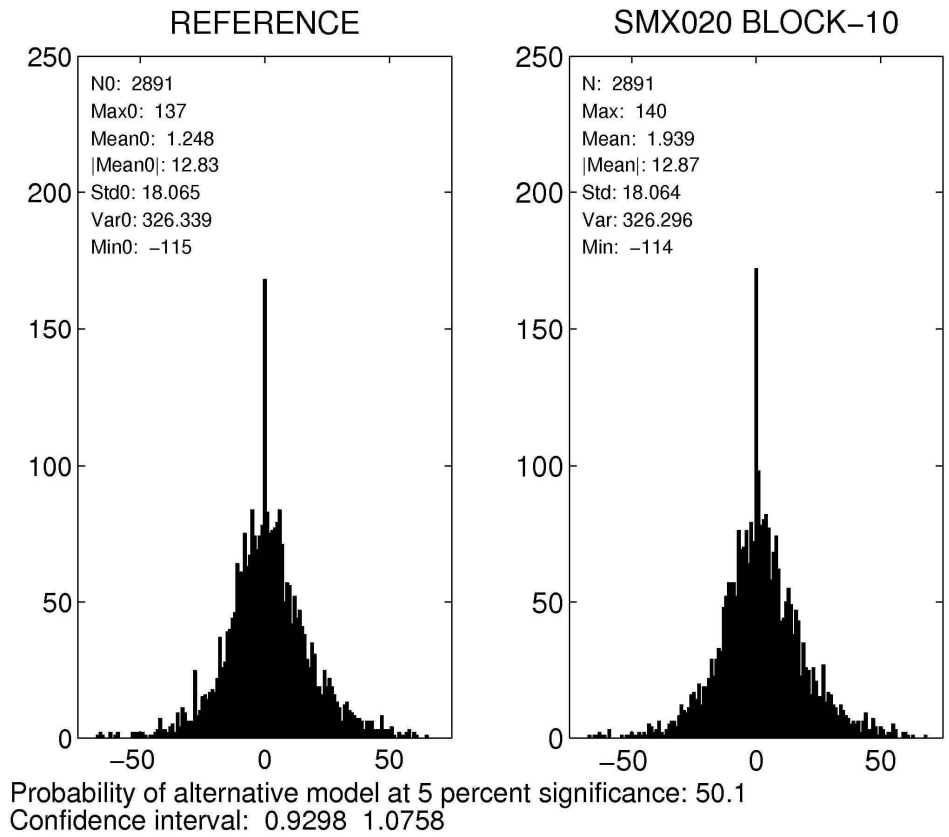

REFERENCE
SMX020 BLOCK−10
N0: 2891
Max0: 137
Mean0: 1.248
|Mean0|: 12.83
Std0: 18.065
Var0: 326.339
Min0: −115
N: 2891
Max: 140
Mean: 1.939
|Mean|: 12.87
Std: 18.064
Var: 326.296
Min: −114
250
200
150
100
50
0
−50
0
50
Probability of alternative model at 5 percent significance: 50.1
Confidence interval: 0.9298 1.0758

Figure 2c

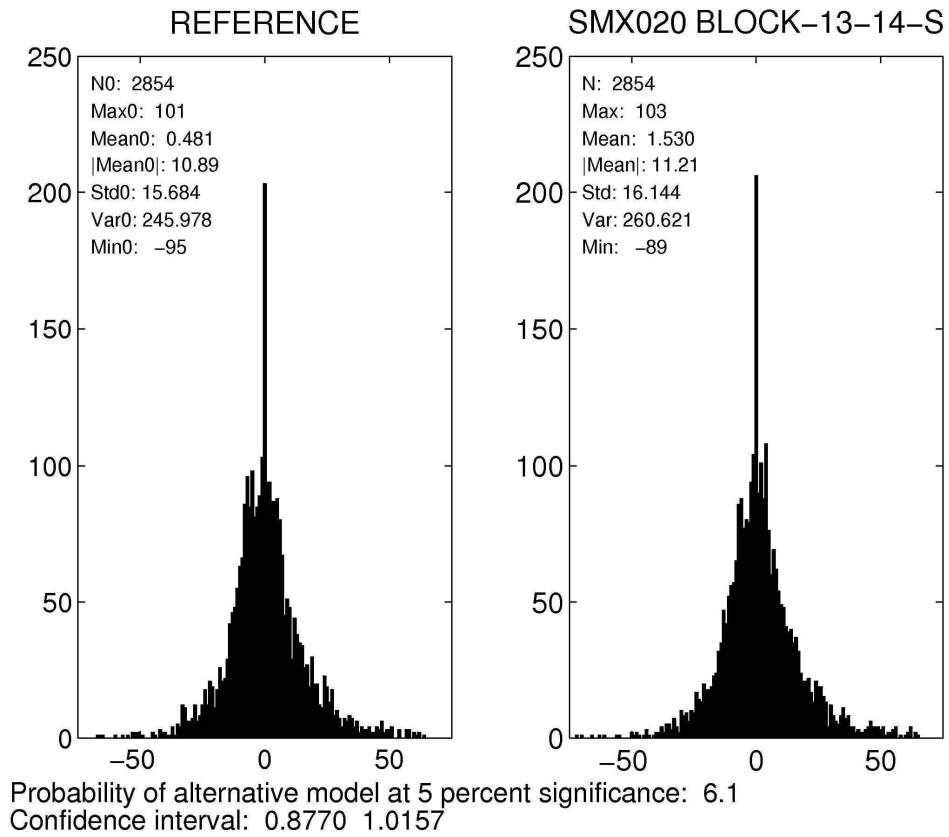

REFERENCE
SMX020 BLOCK−13−14−S
N0: 2854
Max0: 101
Mean0: 0.481
|Mean0|: 10.89
Std0: 15.684
Var0: 245.978
Min0: −95
N: 2854
Max: 103
Mean: 1.530
|Mean|: 11.21
Std: 16.144
Var: 260.621
Min: −89
250
200
150
100
50
0
−50
0
50
Probability of alternative model at 5 percent significance: 6.1
Confidence interval: 0.8770 1.0157

Figure 2d

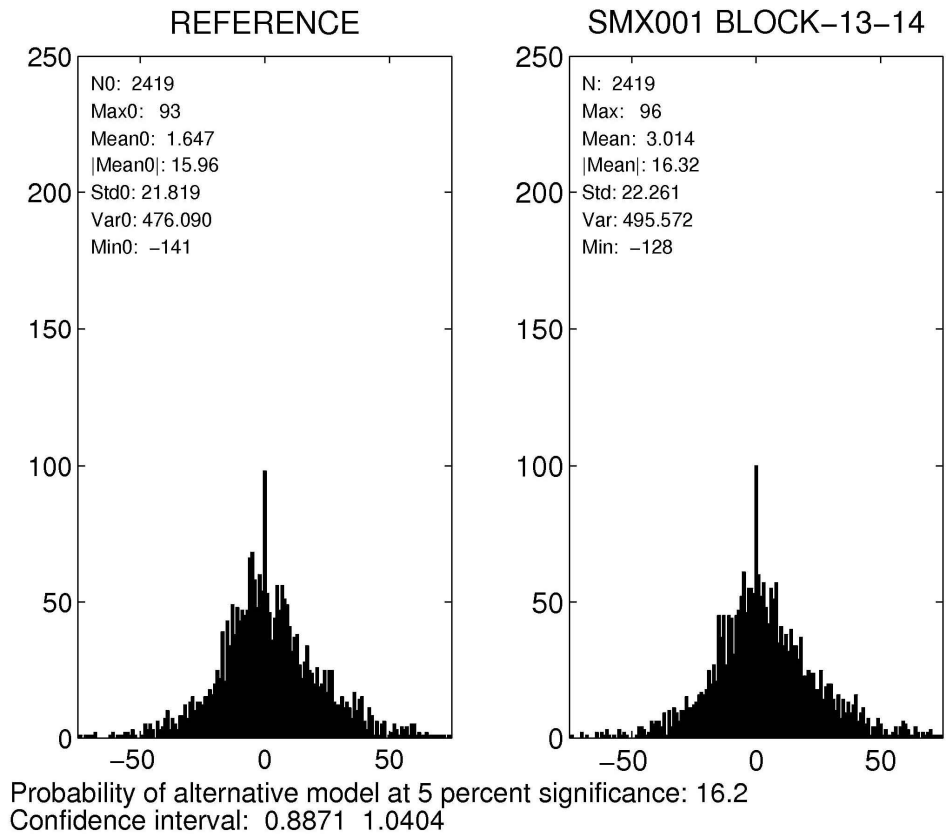

REFERENCE
SMX001 BLOCK−13−14
N0: 2419
Max0: 93
Mean0: 1.647
|Mean0|: 15.96
Std0: 21.819
Var0: 476.090
Min0: −141
N: 2419
Max: 96
Mean: 3.014
|Mean|: 16.32
Std: 22.261
Var: 495.572
Min: −128
250
200
150
100
50
0
−50
0
50
Probability of alternative model at 5 percent significance: 16.2
Confidence interval: 0.8871 1.0404

Figure 3a

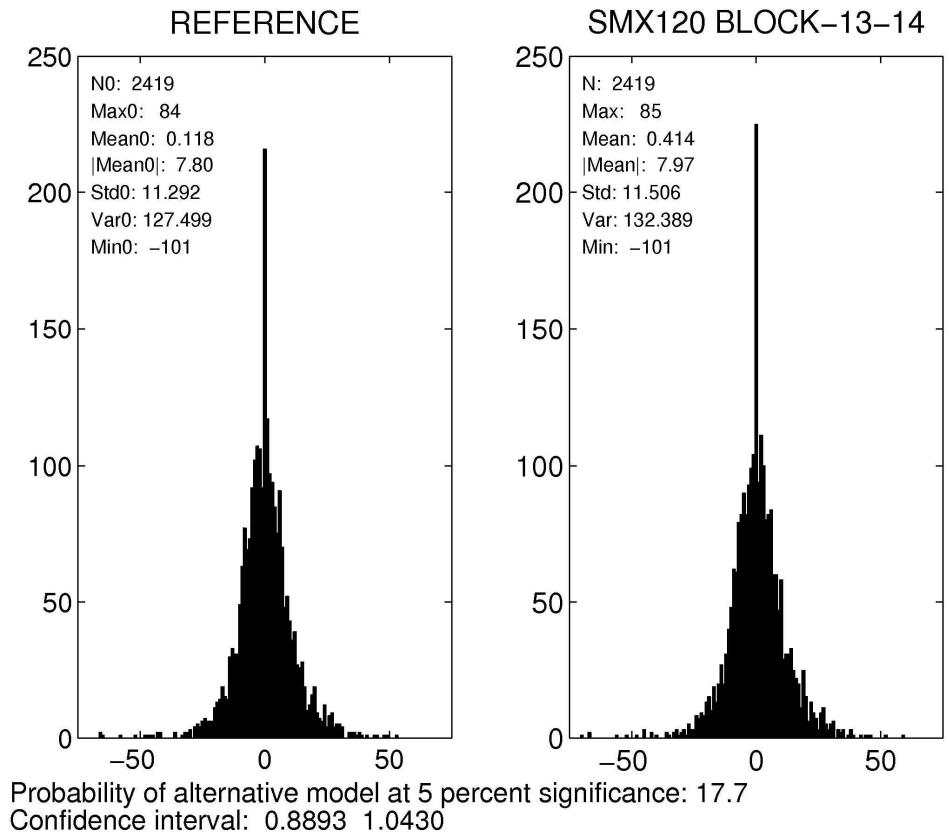

REFERENCE
SMX120 BLOCK−13−14
N0: 2419
Max0: 84
Mean0: 0.118
|Mean0|: 7.80
Std0: 11.292
Var0: 127.499
Min0: −101
N: 2419
Max: 85
Mean: 0.414
|Mean|: 7.97
Std: 11.506
Var: 132.389
Min: −101
250
200
150
100
50
0
−50
0
50
Probability of alternative model at 5 percent significance: 17.7
Confidence interval: 0.8893 1.0430

Figure 3b

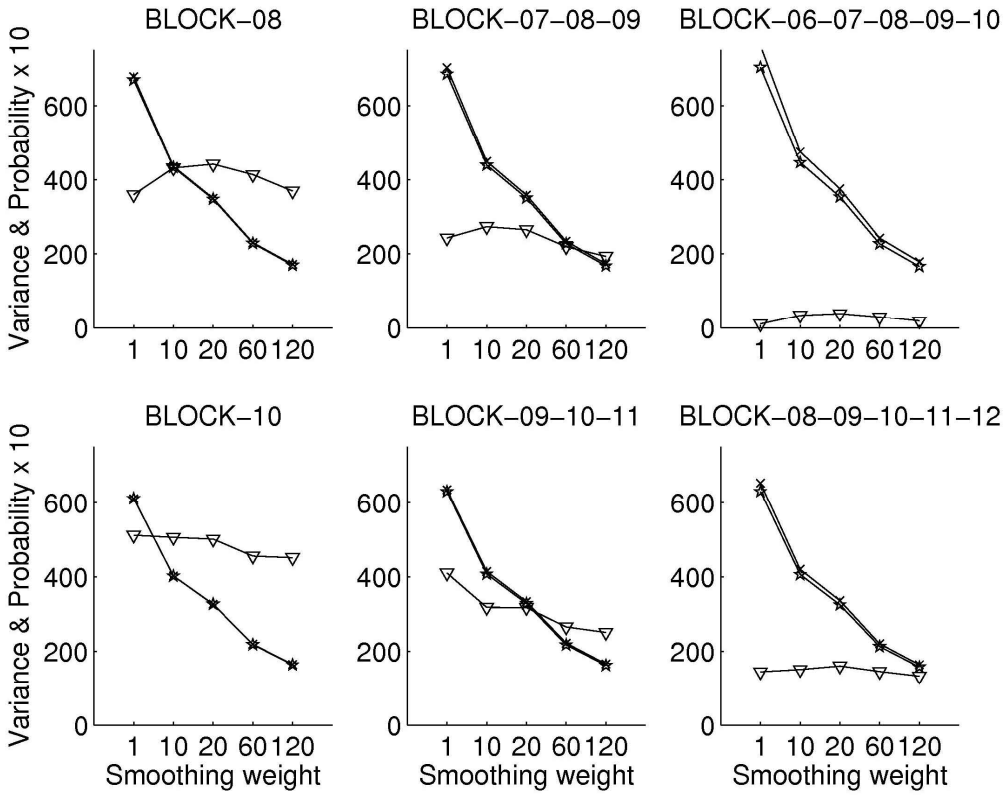

BLOCK–08
BLOCK–07–08–09
BLOCK–06–07–08–09–10
BLOCK–10
BLOCK–09–10–11
BLOCK–08–09–10–11–12
Variance & Probability x 10
0
200
400
600
1 10 20 60 120
Smoothing weight

Figure 4a

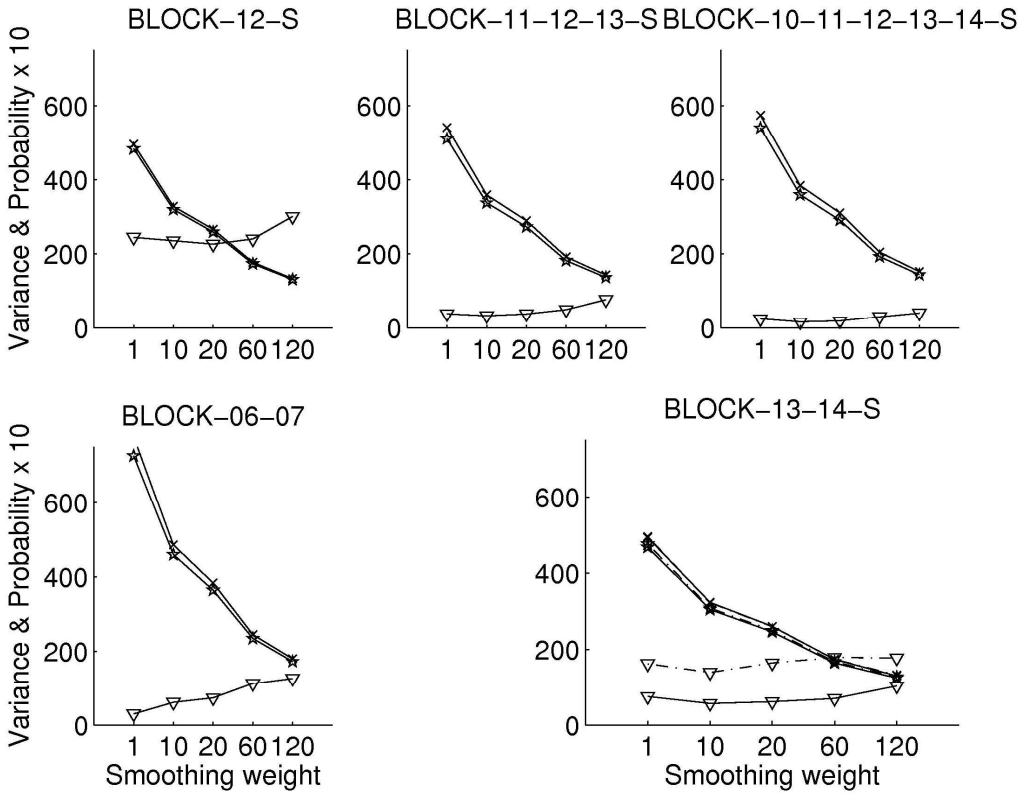

BLOCK−12−S
BLOCK−11−12−13−S
BLOCK−10−11−12−13−14−S
BLOCK−06−07
BLOCK−13−14−S
Variance & Probability x 10
0
200
400
600
1 10 20 60 120
Smoothing weight

Figure 4b

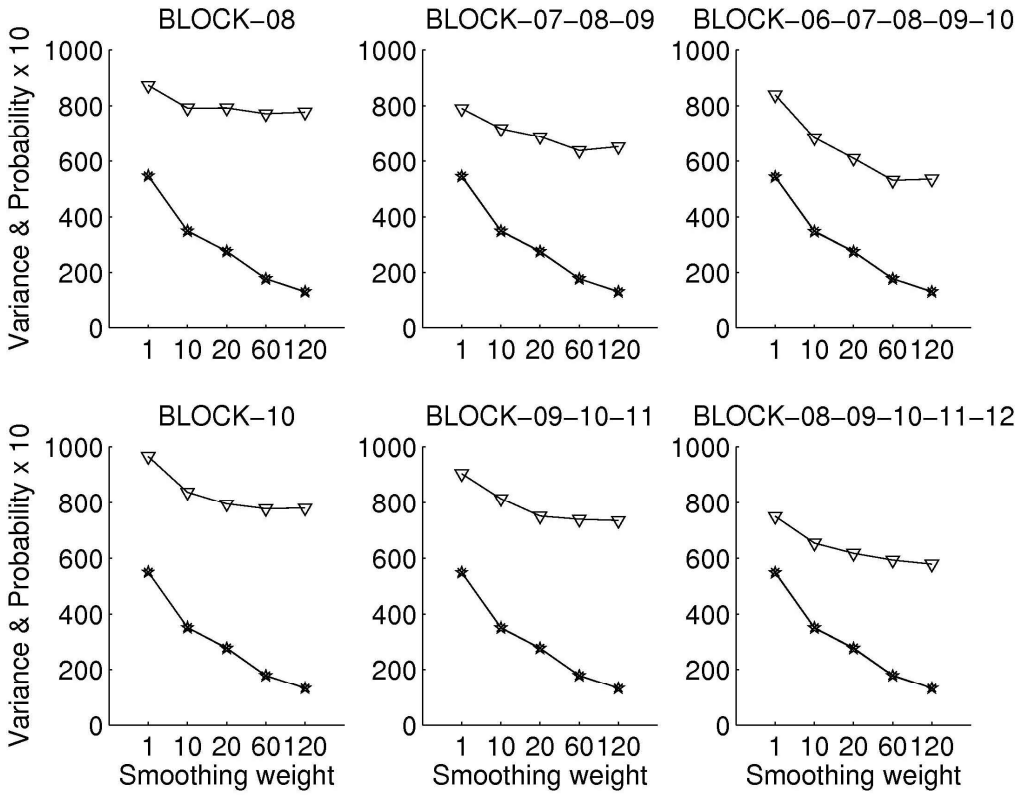

BLOCK–08
BLOCK–07–08–09
BLOCK–06–07–08–09–10
BLOCK–10
BLOCK–09–10–11
BLOCK–08–09–10–11–12
Variance & Probability x 10
Smoothing weight
1000
800
600
400
200
0
1 10 20 60120

Figure 5a

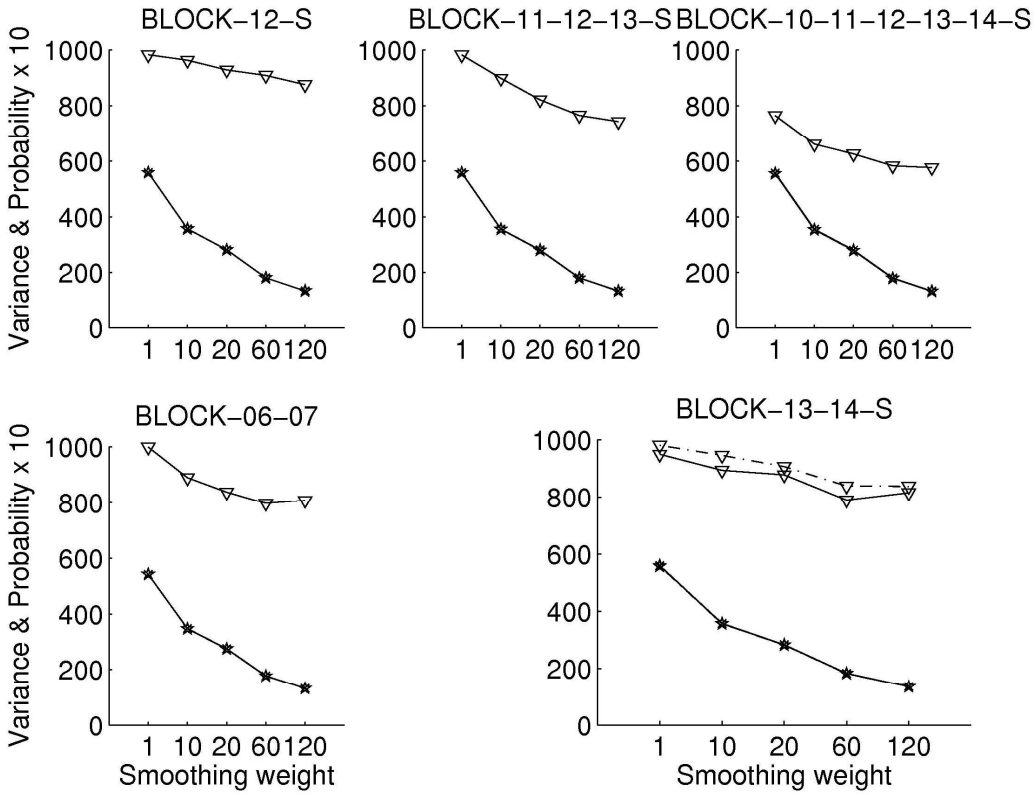

BLOCK−12−S
BLOCK−11−12−13−S
BLOCK−10−11−12−13−14−S
BLOCK−06−07
BLOCK−13−14−S
Variance & Probability x 10
Smoothing weight
1000
800
600
400
200
0
1 10 20 60 120

Figure 5b

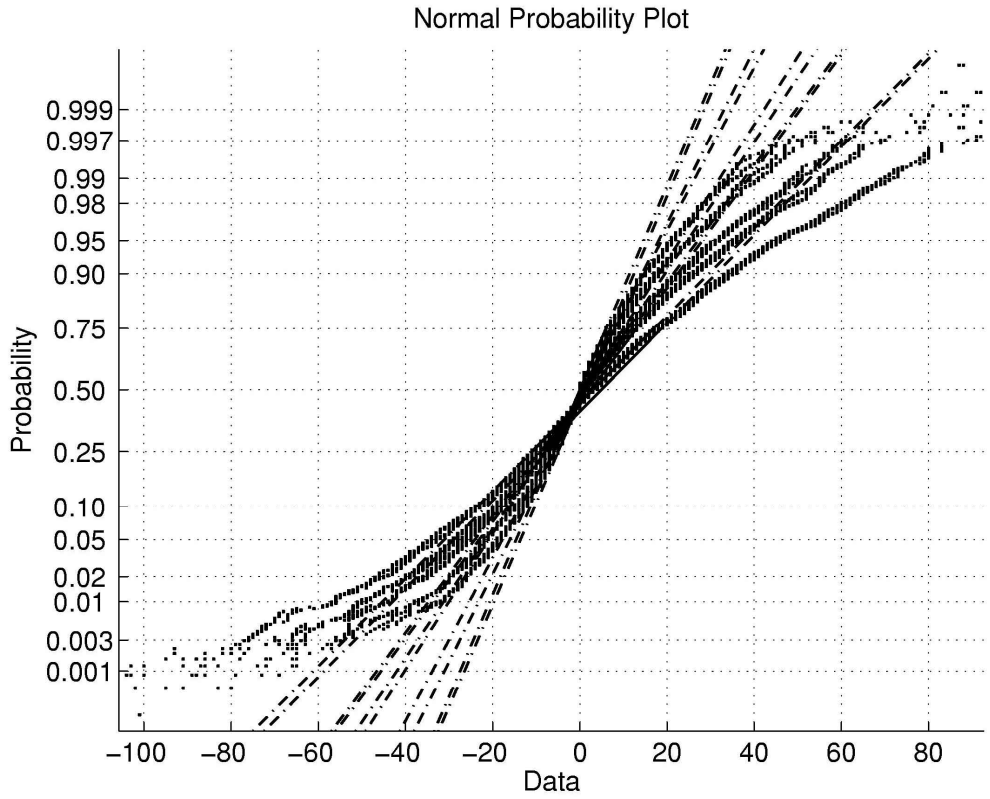
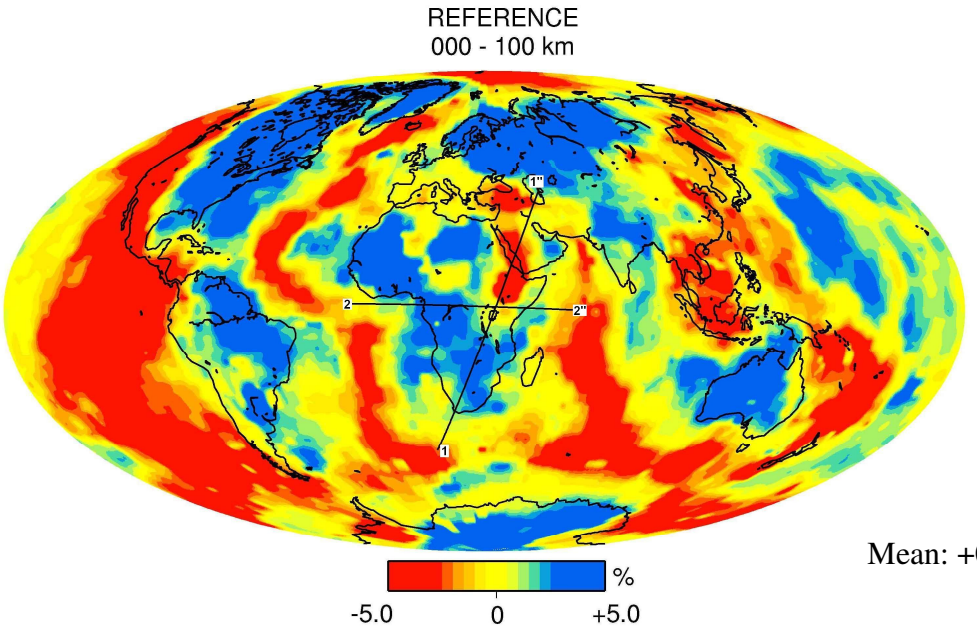
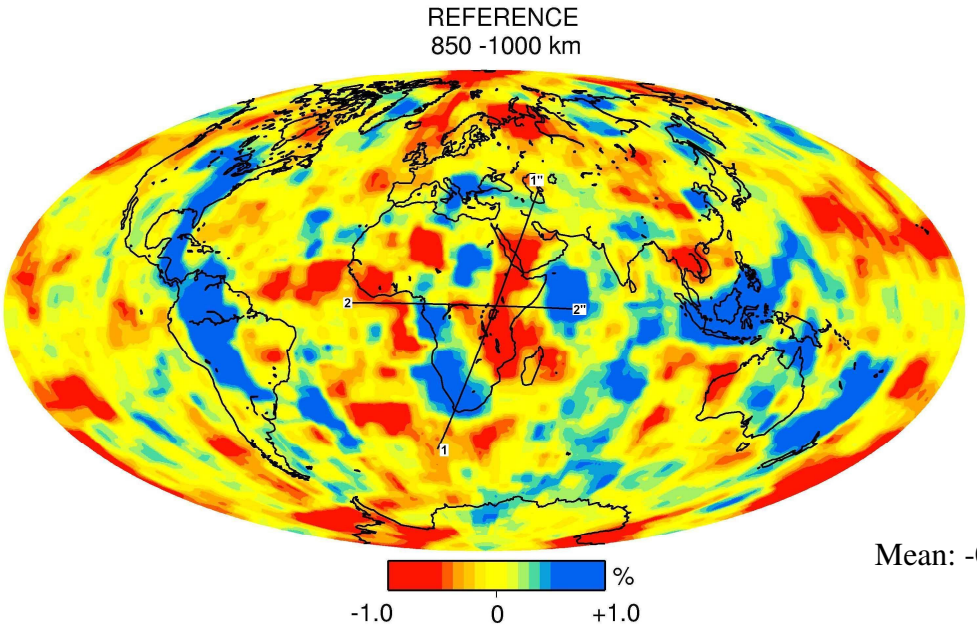

Normal Probability Plot
Probability
0.999
0.997
0.99
0.98
0.95
0.90
0.75
0.50
0.25
0.10
0.05
0.02
0.01
0.003
0.001
−100
−80
−60
−40
−20
0
20
40
60
80
Data

Figure 6



Mean: +0.23%

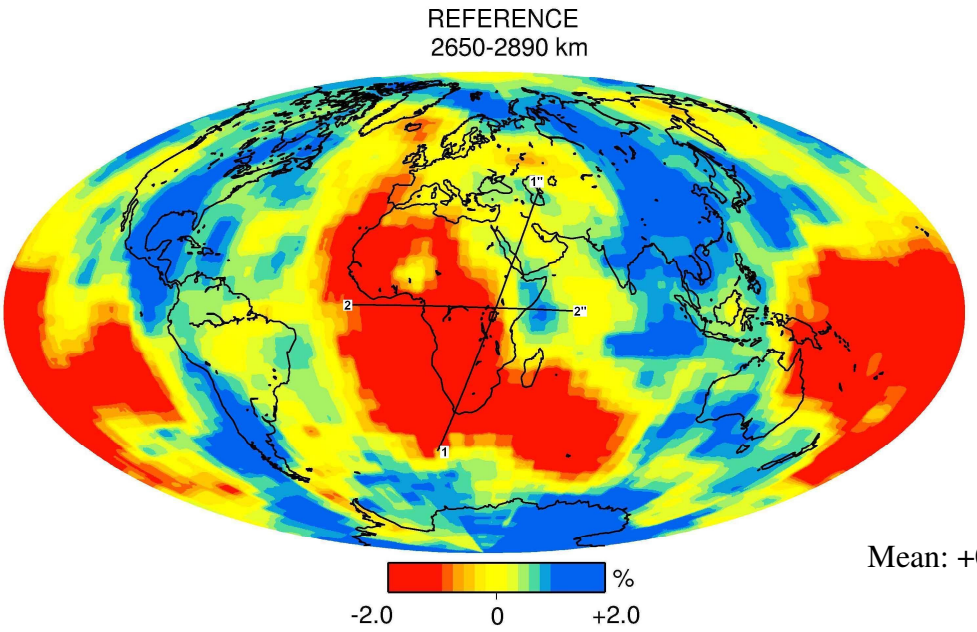
a



Mean: -0.04%

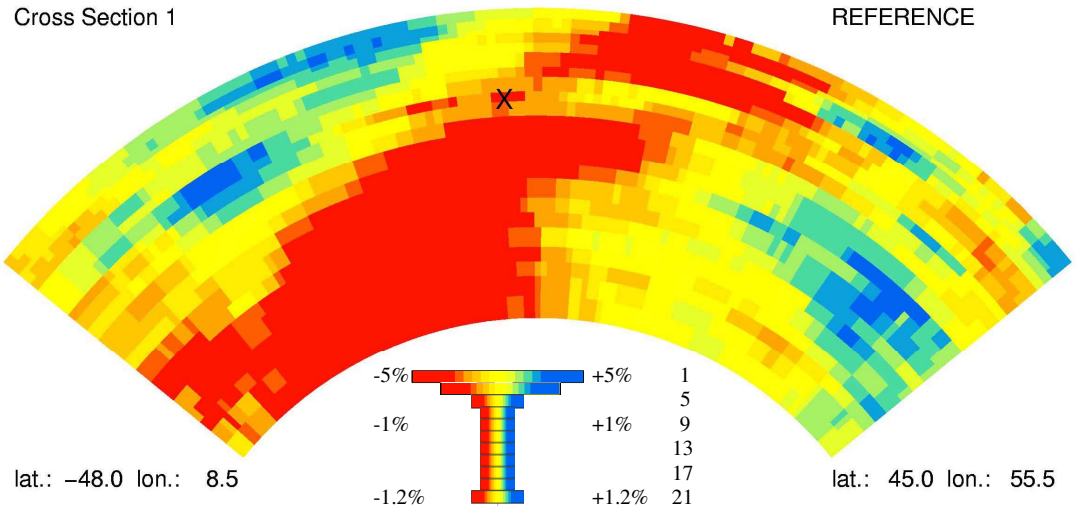
b

Plate A.



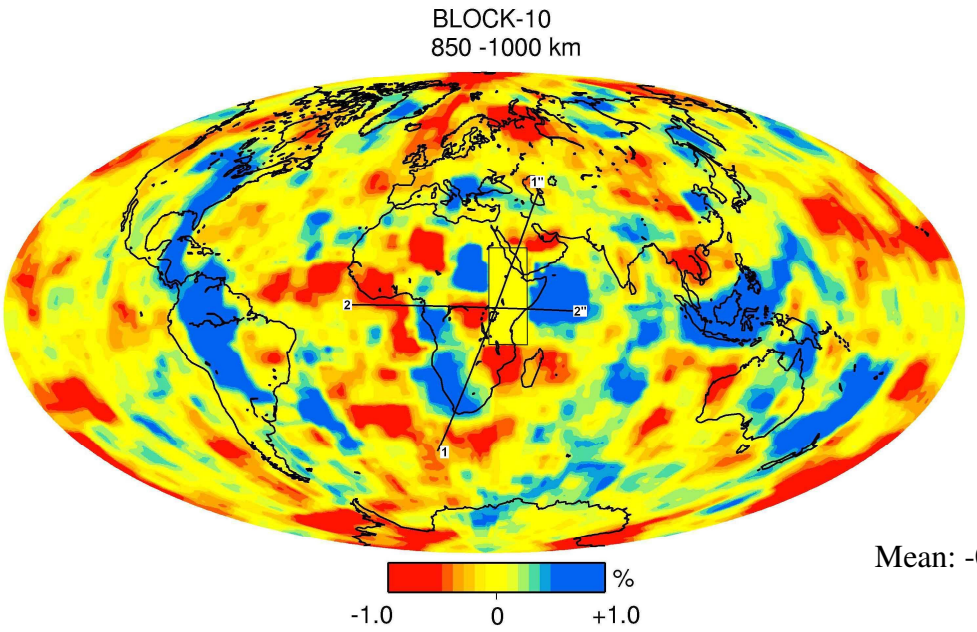
Mean: +0.27%

c



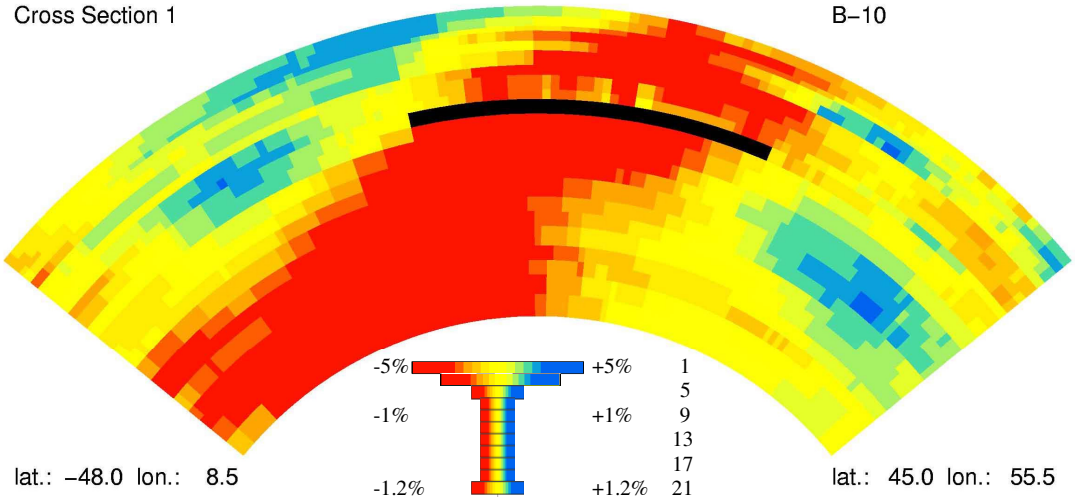
d

Plate A (Continued)



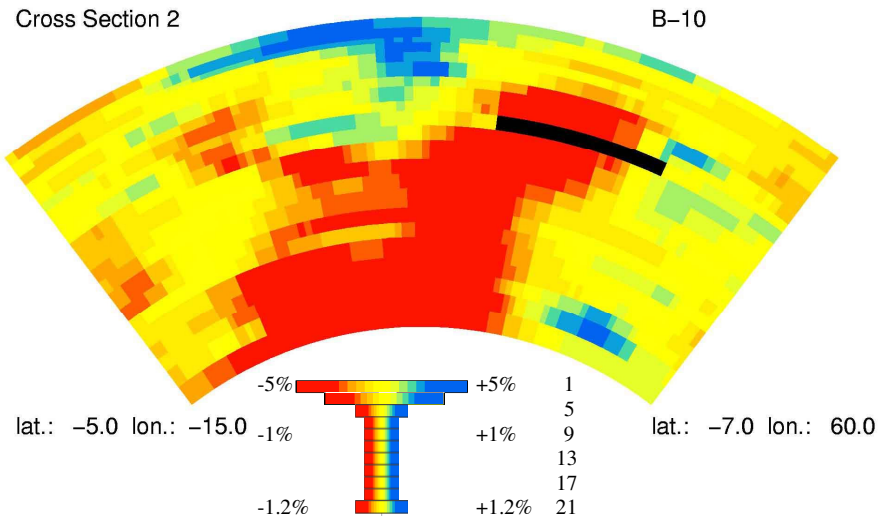
Mean: -0.04%

a



b

Plate B.



c

Plate B (Continued)

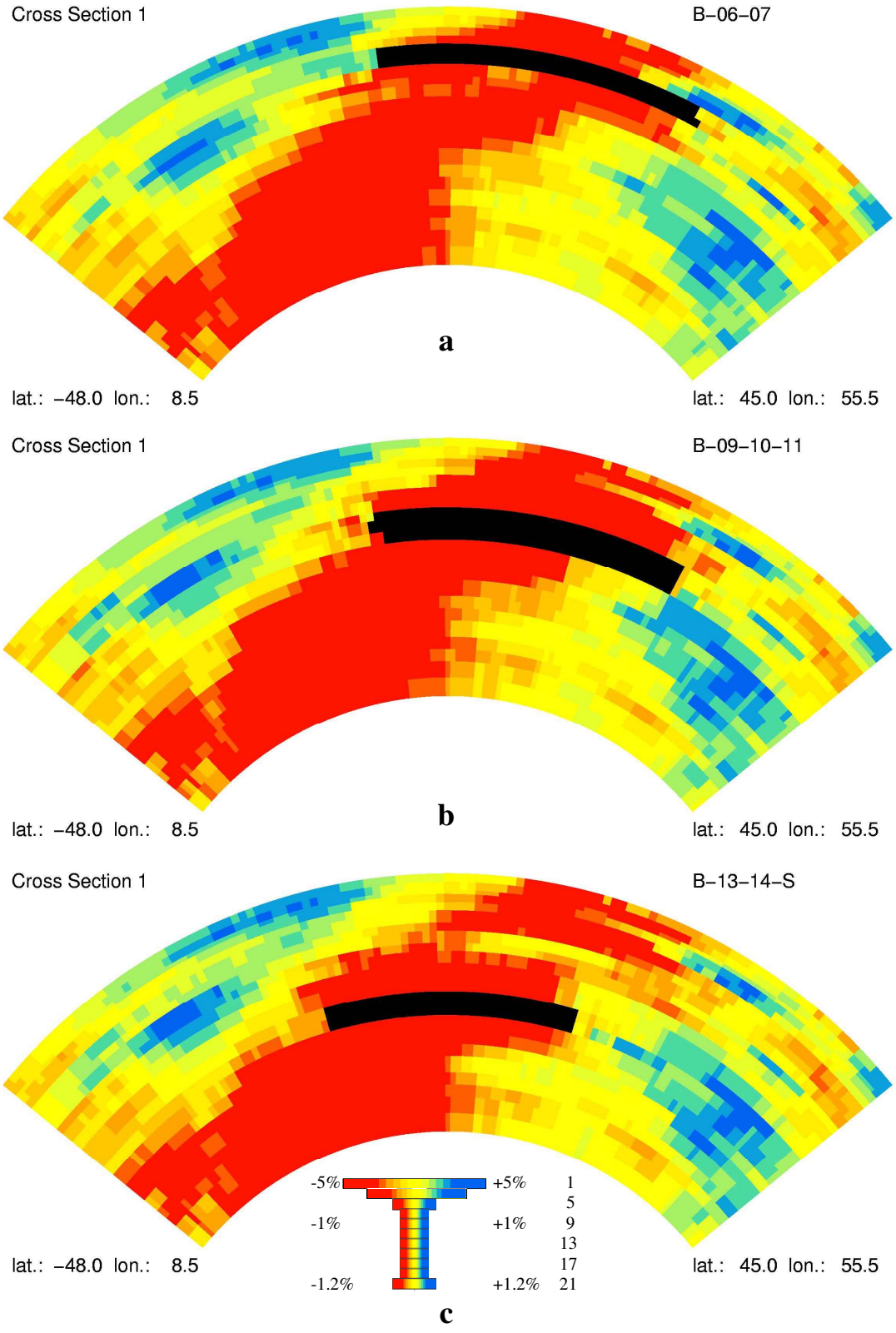

Cross Section 1
B–06–07
a
lat.: –48.0 lon.: 8.5
lat.: 45.0 lon.: 55.5
Cross Section 1
B–09–10–11
b
lat.: –48.0 lon.: 8.5
lat.: 45.0 lon.: 55.5
Cross Section 1
B–13–14–S
-5%
+5%
1
5
-1%
+1%
9
13
17
-1.2%
+1.2%
21
c
lat.: –48.0 lon.: 8.5
lat.: 45.0 lon.: 55.5

Plate C.

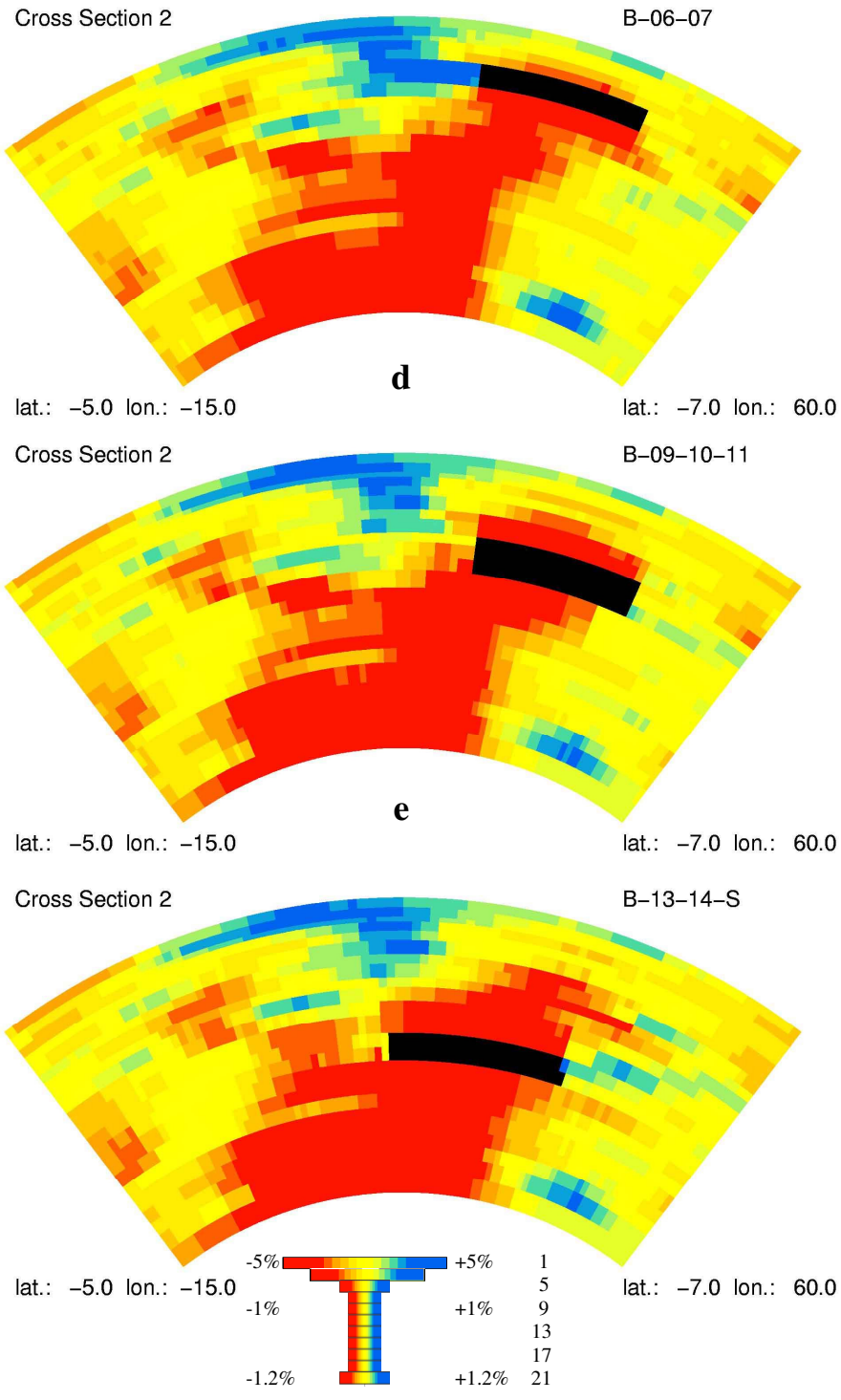
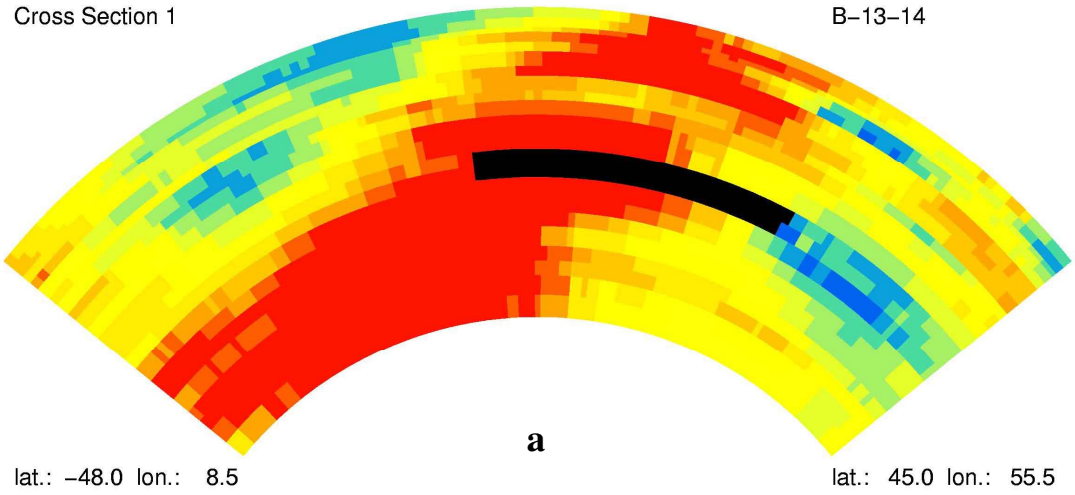
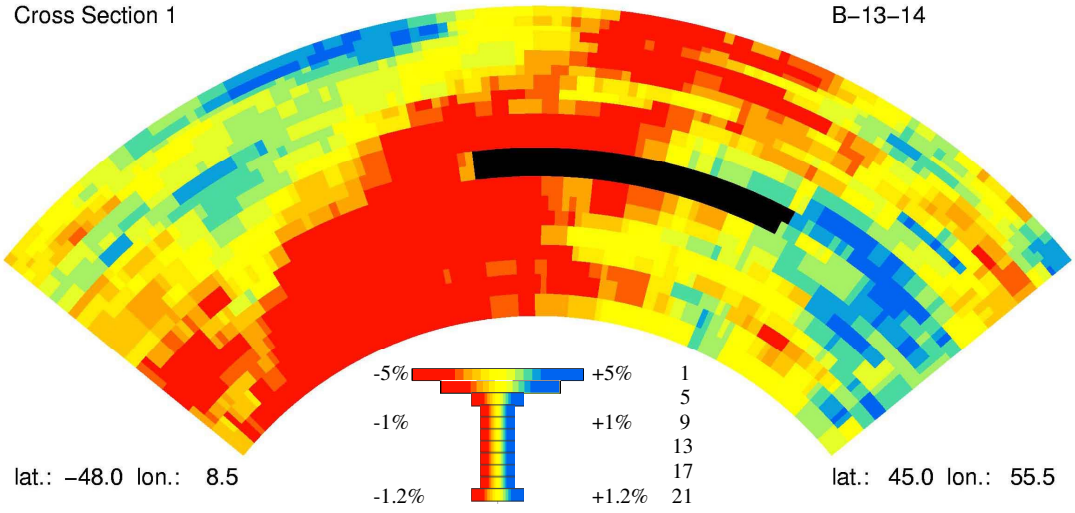


Plate C (Continued)


Cross Section 1
B–13–14
lat.: –48.0 lon.: 8.5
lat.: 45.0 lon.: 55.5

a


Cross Section 1
B–13–14
-5%
+5%
-1%
+1%
-1.2%
+1.2%
1
5
9
13
17
21
lat.: –48.0 lon.: 8.5
lat.: 45.0 lon.: 55.5

b

Plate D.